High Power Laser Science and Engineering, (2025), Vol. 13, e13, 7 pages.
doi:10.1017/hpl.2025.4

HIGH POWER LASER SCIENCE AND ENGINEERING

RESEARCH ARTICLE

Ultrafast characterization of plasma critical surface evolution in inertial confinement fusion experiments with chirped laser pulses

Linjun Li[1,2,†], Zhantao Lu[1,2,†], Xinglong Xie[1,2], Meizhi Sun[1,†], Xiao Liang[1], Qingwei Yang[1], Ailin Guo[1], Ping Zhu[1], Xuejie Zhang[1], Dongjun Zhang[1], Hao Xue[1,2], Guoli Zhang[1,2], Rashid Ul Haq[1,2], Haidong Zhu[1], Jun Kang[1], and Jianqiang Zhu[1,2]

[1]*National Laboratory on High Power Laser and Physics, Shanghai Institute of Optics and Fine Mechanics, Chinese Academy of Sciences, Shanghai, China*

[2]*Center of Materials Science and Optoelectronics Engineering, University of Chinese Academy of Sciences, Beijing, China*

(Received 25 October 2024; revised 22 November 2024; accepted 25 December 2024)

Abstract

Laser-driven inertial confinement fusion (ICF) diagnostics play a crucial role in understanding the complex physical processes governing ICF and enabling ignition. During the ICF process, the interaction between the high-power laser and ablation material leads to the formation of a plasma critical surface, which reflects a significant portion of the driving laser, reducing the efficiency of laser energy conversion into implosive kinetic energy. Effective diagnostic methods for the critical surface remain elusive. In this work, we propose a novel optical diagnostic approach to investigate the plasma critical surface. This method has been experimentally validated, providing new insights into the critical surface morphology and dynamics. This advancement represents a significant step forward in ICF diagnostic capabilities, with the potential to inform strategies for enhancing the uniformity of the driving laser and target surface, ultimately improving the efficiency of converting laser energy into implosion kinetic energy and enabling ignition.

Keywords: critical surface evolution; direct drive; inertial confinement fusion; laser–plasma interaction; plasma diagnostic techniques

1. Introduction

The exploration of controlled fusion energy has been ongoing for more than half a century[1]. Laser inertial confinement fusion (ICF) is one of the most promising paths to achieve thermonuclear ignition, and has achieved tremendous advancements in both scientific understanding and engineering aspects[2]. The first laboratory achievement of target gain $G_{\text{target}} > 1$ was reported at the US National Ignition Facility (NIF) in December 2022[3], demonstrating the potential of the laboratory fusion. Both direct and indirect drives typically employ spherical targets. As the target surface absorbs laser energy and undergoes ablation, the pressure causes the remaining ablation layer and the deuterium–tritium (DT) fuel shell to implode inward. When the implosion reaches its minimum radius, a hot spot of DT forms, surrounded by colder, denser DT fuel[4]. Low-mode asymmetries are the dominant factor that degrades implosion performance. In addition, mixing of the ablation layer and the fuel also causes significant fuel preheating, further degrading implosion performance[2]. Improving the coupling of laser energy into target kinetic energy is a key to achieve the ignition. Laser–plasma instabilities[5], that arise from the interaction between the driving laser and the ablation plasma, can limit the absorption of laser energy and also accelerate electrons to the DT fuel layer, thereby reducing the final compression and preventing the ignition process[6]. Precise shaping and control of the driving laser pulse is a key step in the ICF process to reduce Rayleigh–Taylor (RT) instabilities and improve energy coupling efficiency[7]. When the laser interacts with the ablation layer, a critical surface is formed, and most of the laser energy is absorbed by the coronal region due to reflection at this critical surface, limiting

Correspondence to: X. Xie and J. Zhu, National Laboratory on High Power Laser and Physics, Shanghai Institute of Optics and Fine Mechanics, Chinese Academy of Sciences, No. 390 Qinghe Road, Jiading District, Shanghai 201800, China. Emails: xiexl329@siom.ac.cn (X. Xie); jqzhu@siom.ac.cn (J. Zhu)

[†]These authors contributed equally to this work.

the effective conversion to implosion kinetic energy[1,2,4–7]. We believe that understanding the evolution of the critical surface during the laser–ablation layer interaction will play an important role in improving the conversion efficiency of laser energy to fuel kinetic energy. Therefore, exploring the temporal evolution of the critical surface can provide a guidance for controlling the driving laser, adjusting the laser pulse pointing and designing the target, laying the foundation for ultimately achieving ignition.

To explore the complex physical processes in ICF and improve the coupling of laser energy to the target, various diagnostic techniques have been developed, such as VISAR[8], X-ray imaging[9] and X-ray spectroscopy[10]. VISAR measures the velocity of moving surfaces by recording the Doppler shift of the reflected light. VISAR is a critical diagnostic tool in ICF and high-energy-density research, as it can be used to measure the velocity of rapidly moving surfaces (typically from ~0.1 to >100 km/s)[11–15], measure equations of state[16], characterize the strength and structure of materials under extreme conditions[17] and optimize the temporal pulse shape of the implosion laser in ICF experiments[18]. X-ray imaging can record the information about the shape, volume and temperature of the plasma, providing valuable feedback for adjusting experimental parameters. Pinhole imaging is the most commonly used X-ray imaging diagnostic, as pinholes are easy to fabricate and position, and can be easily replaced if damaged[19]. The principle of pinhole X-ray imaging is similar to that of visible light pinhole imaging, and the spatial resolution is limited by geometric optics and diffraction. X-ray spectroscopy can be used to diagnose the mixing of ablator material into the hot spot in indirect-drive experiments[20] and to characterize the state of the target[21].

Many of the aforementioned diagnostic techniques often work with streak cameras and rely on algorithmic reconstruction to obtain plasma parameters. Furthermore, existing diagnostic methods tend to focus on the compressed core region, lacking diagnostics for the critical surface of the ablation plasma. We believe that the lack of understanding of the evolution of the plasma critical surface hinders the improvement of laser energy coupling efficiency. In this paper, we propose an all-optical diagnostic method based on ultrashort lasers to diagnose the critical surface formed by the interaction between the driving laser and the ablation layer in the ICF process, and experimentally verify the feasibility of the method.

2. Methods

We have developed a femtosecond laser-based fusion plasma measurement method. This method utilizes the rich frequency components of femtosecond lasers, using dispersion to temporally stretch the probe pulse, thus making a probe

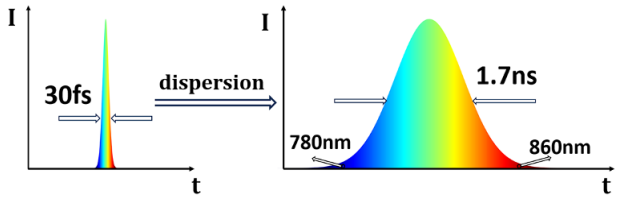

Figure 1. A femtosecond laser pulse with a center wavelength of 808 nm and a pulse duration of 30 fs is coupled into a pulse stretcher. The pulse stretcher introduces group velocity dispersion, which stretches temporally the pulse duration by frequency–time chirp. This results in the generation of a chirped probe pulse with a duration of 1.7 ns and a spectral range of 780–860 nm. The time-dependent wavelength distribution of this stretched probe pulse allows for time-resolved probing of the evolving plasma dynamics under investigation.

with time–frequency chirp, as shown in Figure 1. We use a pulse with a center wavelength of 808 nm and a pulse width of 30 fs, which is then stretched to 1.7 ns by a pulse stretcher, with a spectral range of 780–860 nm. It is a flat-top s-polarized pulse with a fast rise of approximately 100 ps. This probe beam is then made to interact with the evolving plasma under study, where different wavelengths can record information at different time instants. Finally, we record the spectral changes of the probe beam before and after the measurements, and by analyzing these changes, we can obtain the expansion velocity of the critical surface as well as the time-resolved evolution of the critical surface morphology.

In a linearly temporally stretched femtosecond laser pulse, different time points correspond to different wavelengths. When this chirped probe pulse interacts with the critical surface, the spectral components of the measured probe pulse are recorded using a spectrometer. By analyzing and comparing the spectral changes of the probe pulse before and after the interaction with the critical surface, the evolution dynamics of the critical surface within the probe pulse duration can be obtained. To evaluate the velocity of the critical surface, the probe beam is first compressed to a narrow pulse of several tens of femtoseconds using a parallel grating compressor, and the pulse width is measured using an autocorrelator before the probe beam interacts with the plasma critical surface. After the probe beam interacts with the plasma, it is compressed again using the same parallel grating compressor, and the change in the probe beam pulse width Δt can be measured. This change in pulse width Δt reflects the expansion velocity v of the plasma critical surface. By analysis, a relationship can be established among the change in pulse width Δt, the probe beam pulse width τ, the incidence angle θ and the critical surface expansion velocity v, as shown in the following equation:

$$\Delta t = \frac{2v\tau}{\cos\theta \times c}, \tag{1}$$

where c is the speed of light. The charge-coupled device (CCD) image recorded captures the temporal evolution of the critical surface topography. The spatial information on the CCD corresponds to the temporal evolution of the critical surface, with each position on the CCD representing a different time delay relative to the initial probe pulse.

3. Experimental setup

The experiment is conducted at the SG-II nanosecond laser facility and SG-5PW femtosecond laser system. The probe beam employed in our experiment is sourced from the SG-5PW front-end and expanded to about 100 mm × 100 mm in size[22–24], in which two optical parametric chirped pulse amplification (OPCPA) links make up the whole beam, and each of the OPCPA links has two beta barium borate (BBO) crystals. These BBO crystals are cutting in Type 1 configuration, with a phase matching angle of 23.8° and a non-collinear angle of 2.36° within the crystal. The frequency-doubled neodymium-doped yttrium aluminum garnet (Nd:YAG) laser independently developed by our laboratory is used as the pump source of the OPCPA links at a repetition rate of 1 Hz. The femtosecond seed pulse is generated by a commercial Ti:sapphire laser (Femtosecond Lasers). The seed pulse width is 10 fs, the repetition rate is 75 MHz and the average power is 150 mW. After passing through the stretcher, the seed pulse is temporally broadened into a chirped pulse with a full width at half maximum (FWHM) of 0.85 ns and a chirp rate of 21.3 ps/nm.

The experimental setup utilizes one beam of the SG-II, a 526 nm, 1 ns, 200 J laser pulse as the driving laser. It drives the formation of fusion plasma from a carbon-deuterium (CD) target (a commonly used low-Z ablator material in ICF experiments). The focused peak power density is 1×10^{15} W/cm^2. The temporal profile of the drive laser is a square wave, with a rise time of approximately 110 ps. The probe beam is a chirped pulse, as mentioned in the previous section. As shown in Figure 2, this time-resolved imaging technique leverages the interaction between the probe beam and the plasma critical surface. The driving beam is incident vertically on the target surface, while the probe beam is focused by an off-axis parabolic mirror and incident on the target surface at an angle of 21°. In the experiment, the time synchronization between the drive laser and the probe beam was measured at the target location using a photodetector. The photodetector's response time is 60 ps, and the accuracy of the time synchronization is 10 ps root mean square (RMS). The time delay mentioned in the subsequent text refers to the temporal difference between the leading edges of the two laser pulses.

After interacting with the fusion plasma, the probe beam is collimated by lens L1 and reflected by mirror M2 to be extracted from the vacuum target chamber. The probe beam is then split by beam splitter BS1, with one portion

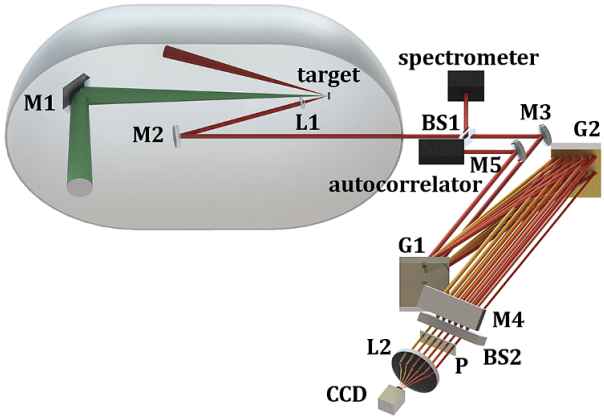

Figure 2. The experimental setup consists of the following optical components: M1–M7 are reflective mirrors, BS1 and BS2 are beam splitters, L1 and L2 are focusing lenses, G1 and G2 are gold-coated diffraction gratings and P is an aperture plate. Notably, M1, M2 and the target are all situated within a vacuum target chamber.

directed to a spectrometer to measure the probe spectrum. The other reflected by M3 is sent through a pair of diffraction gratings G1 and G2 to recompress the probe beam back to its original femtosecond pulse duration, which is then reflected by mirror M4 and directed into an autocorrelator to measure the pulse width of the compressed probe beam. The remaining portion of the probe beam is diffracted by the grating pair G1 and G2, collimated and transmitted through BS2. This beam then passes through an aperture plate P (with six pinholes corresponding to wavelengths of 809, 815, 821, 826, 833 and 837 nm) and lens L2, and is imaged onto a CCD camera. By comparing the brightness of the spots on the CCD before and after the injection of the drive beam, the synchronization between the drive and probe beams can be assessed, providing a reference for adjusting the time delay between the two beams.

4. Results and discussion

In order to further analyze the experimental data, we utilized the radiation magnetohydrodynamics code FLASH[25,26] to perform simulations. FLASH is capable of multi-temperature treatment of the plasma, enabling it to model high-energy-density physics experiments driven by lasers. Based on the laser and target parameters in the experiment, we conducted laser-driven ablation simulations on a 50 μm thick, 1 g/cm^3 density CD target using a 526 nm wavelength, 1×10^{15} W/cm^2 intensity, 1 ns duration laser. The initial setup of the simulation is shown in Figure 3. The simulation domain size was 280 μm × 80 μm with a grid size of 0.1 μm. Subsequently, we reconstructed the experimental optical path of the probe beam.

At time t, the probe beam wavelength components λ were incident on the laser-ablated plasma at uniform angles θ ranging from 16° to 26°. The different wavelengths λ and

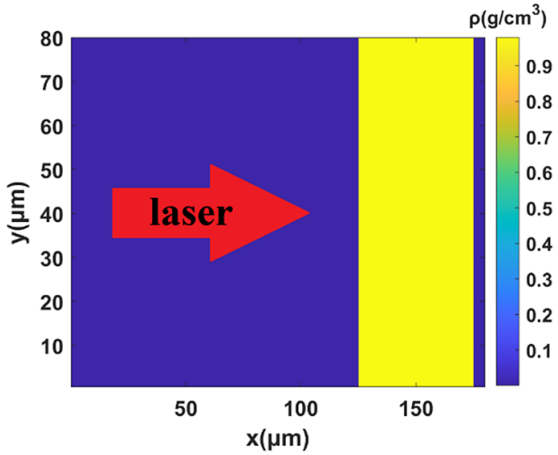

Figure 3. The initial conditions for the simulation.

incident angles θ correspond to different densities of the reflection surface. Based on the FLASH simulation results, we obtained the critical surface position, velocity, reflectivity and tangential angle (reflecting the critical surface morphology) at that time and location. We then calculated the Doppler shift in wavelength and the reflection angle due to the Doppler effect, and performed ray tracing to determine the portion of the light that could pass through the subsequent optical components and reach the spectrometer, thereby obtaining the simulated spectrometer signal. The results calculated without considering the changes in surface morphology at the critical surface are shown in Figures 4(a), 4(c) and 4(e), where the red line represents the spectrum received by the spectrometer in the experiment, and the blue line shows the calculated spectrum. Without considering the changes in surface morphology, the wavelength range that can reach the spectrometer is very wide, and the periodic peaks and valleys reflect the oscillation of the critical surface driven by the hydrodynamic force. When the changes in surface morphology are considered, the calculated results are shown in Figures 4(b), 4(d) and 4(f), where the red line represents the spectrum received by the spectrometer in the experiment, and the blue line shows the calculated spectrum. The calculated results agree well with the experimental results.

To explain the changes in the spectrum, we consider the critical surface in the probe beam interaction region as a curved arc. In the initial phase of the interaction of the probe with the plasma surface, most of the probe is reflected by the surface, which works like a convex mirror, so only a small part of the light energy enters into the subsequent optical path. After some time, the curvature of the curved arc decreases due to the probe beam's action, and the portion entering the subsequent optical path is maximized. Meanwhile, the reflective mirror formed by the two ends of the curved arc rotates towards the direction perpendicular to the probe beam due to the probe beam's action. After several hundred picoseconds, the reflected probe beam can no longer enter the subsequent optical path due to the change in the reflection angle. The changes in the surface morphology of the critical surface are caused by the actual surface profile of the planar target used in the experiment and the nonuniformity of the driving laser. Therefore, our measurement method can reflect the time-dependent changes in the surface morphology of the critical surface. In addition, it is worth noting that the different spectra at different delays are due to the changes in the position of the critical surface, and the cessation of the driving laser results in the termination of the isothermal expansion, leading to changes in the density distribution of the plasma induced by the rarefaction wave.

The CCD images before and after the drive beam injection are shown in Figure 5.

In the absence of the drive beam injection, the light spot on the CCD corresponds to the reflection of the probe beam from the target surface itself, exhibiting relatively weak brightness. Starting from the image of the fifth hole (corresponding to a wavelength of 815 nm), that is, approximately 750 ps after the probe beam interaction, the brightness of the light spot is significantly reduced due to the damage of the target under laser irradiation. After the drive beam injection, the light spot on the CCD is attributed to the reflection of the probe beam from the plasma critical surface, with a relatively high reflectivity exceeding 70%, resulting in an enhanced brightness of the light spot. Interestingly, we observed that the light spots in the first two holes are larger, while the light spot in the third hole is considerably smaller. Based on the simulation results, this phenomenon can be attributed to the presence of the pre-pulse. The pre-pulse arrives before the probe beam and forms an initial plasma distribution. The probe beam, having a longer wavelength and a lower critical density, corresponds to a relatively flat critical surface morphology. In addition, the low-density region is farther away from the target surface, and the change in object distance leads to a larger image on the CCD. In this case, the light spot on the CCD represents the reflection image of the plasma critical surface within the probe beam range. The main pulse arrives between the time corresponding to the second hole and that corresponding to the third hole. Due to the high light intensity, the plasma within the main pulse light spot is rapidly compressed towards the target surface, while the surrounding plasma is also affected, forming a 'funnel' shape. In this scenario, the light spot on the CCD corresponds to the reflection image of the plasma critical surface within the main pulse light spot, and the other parts within the probe beam range cannot enter the CCD due to the change in the plasma critical surface morphology.

Based on the measurements from the autocorrelation setup, we have calculated the expansion velocity of the critical surface, as shown in Figure 6. Figure 6(a) presents the autocorrelation signals obtained at different delays between the probe beam and the main pulse leading edge,

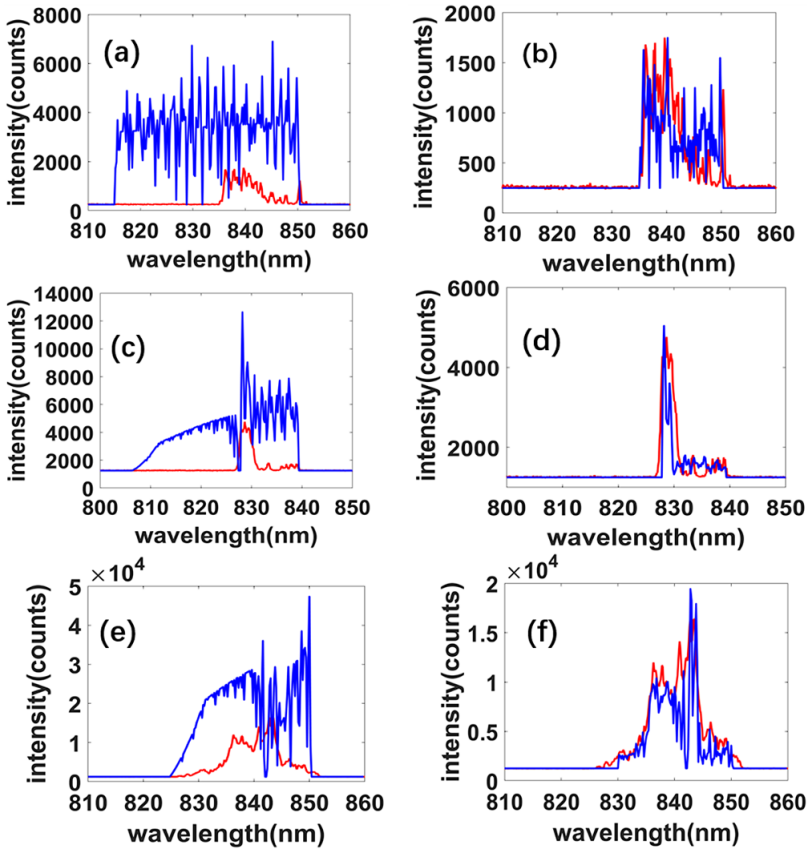

Figure 4. Measured probe beam spectrum (red line) and calculated spectrum (blue line). Without considering the change in the critical surface morphology, the probe beam is delayed relative to the drive beam by (a) 250 ps, (c) 940 ps and (e) 1035 ps. Considering the change in the critical surface morphology, the probe beam is delayed relative to the drive beam by (b) 250 ps, (d) 940 ps and (f) 1035 ps.

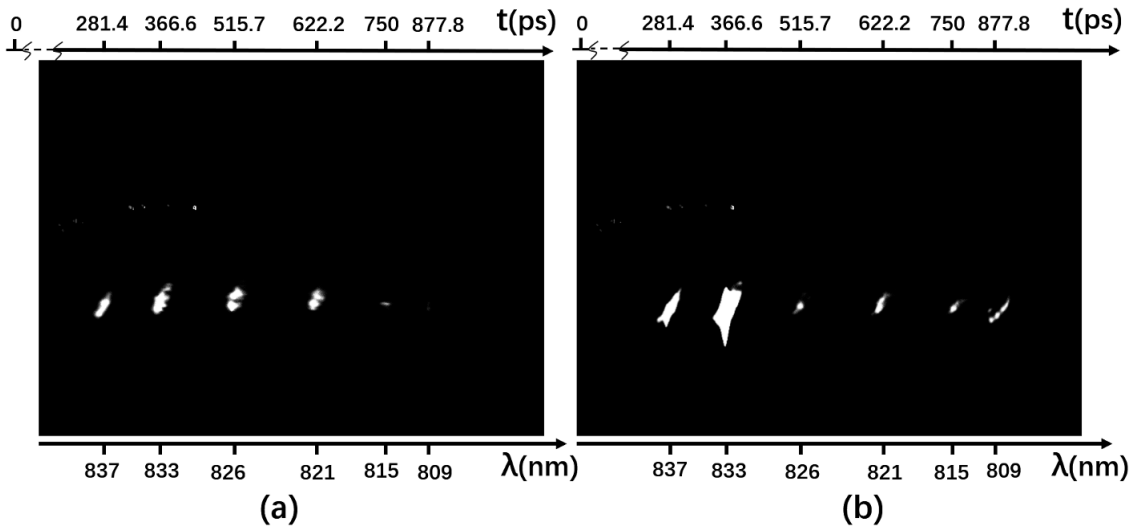

Figure 5. The image on the CCD sensor (a) without the driving laser and (b) with the driving laser. Specifically, the zero-point in the figure represents the moment when the probe beam begins to interact with the target.

where the delay refers to the relative time between the main pulse leading edge and the probe beam leading edge. To avoid the gradual change in the critical surface morphology under the influence of the probe beam, as discussed previously, we have extracted the 836–850 nm portion of the probe beam, corresponding to a broadened pulse width of 300 ps.

Using Equation (1), we can calculate the critical surface expansion velocity at different time points and compare it with the results from numerical simulations, as shown in

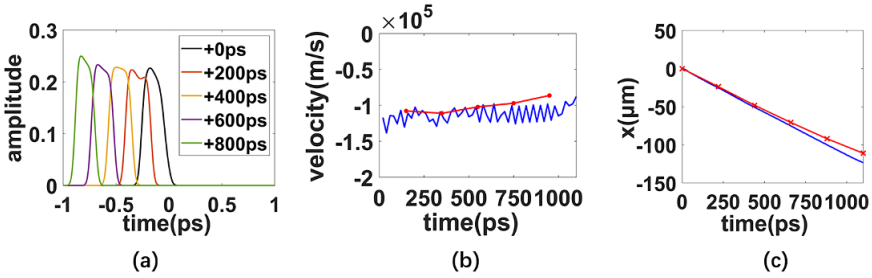

Figure 6. (a) Autocorrelation signals at different time delays (0, 200, 400, 600, 800 ps). (b) Critical surface expansion velocity measured from the autocorrelation signals (red line) and obtained from numerical simulations (blue line). (c) Critical surface position as a function of time measured from the autocorrelation signals (red line) and obtained from numerical simulations (blue line). (The negative sign in Figures 6(b) and 6(c) indicates that the direction of the plasma critical surface movement is opposite to the direction of the drive laser.)

Figure 6(b). The oscillation in the simulated velocity is due to the effect of radiation pressure, which causes the critical surface to oscillate. In contrast, the autocorrelation signal-based velocity represents the average motion of the critical surface within the 300 ps interaction with the probe beam. Furthermore, we have also calculated the critical surface position at different time points based on the measured velocity and compared it with the numerical simulation results, as shown in Figure 6(c). The measured results agree well with the numerical simulation, and the critical surface expansion velocity is in the range of 1×10^5–2×10^5 m/s, consistent with previous reports[22]. The deviations in the results can be attributed to two factors: firstly, the measurement error of the autocorrelation setup and, secondly, the fact that for the 836–850 nm probe beam, the shorter wavelength part corresponds to a higher critical density and is reflected at a position closer to the target, resulting in a smaller change in the optical path compared to the case where the wavelength is constant, leading to an underestimation of the critical surface expansion velocity.

5. Conclusions

We have developed a novel optical measurement technique capable of probing the surface deformation and expansion velocity of the critical surface within the ablation layer during the ICF process. This innovative approach provides new insights into the underlying physical phenomena governing ICF, which can inform strategies to enhance the uniformity of the drive laser and target surface. Ultimately, this advancement has the potential to improve the efficiency of converting laser energy into implosion kinetic energy.

Acknowledgements

This work was supported by the National Natural Science Foundation of China (NSFC) (12074399, 12204500 and 12004403), the Key Projects of Intergovernmental International Scientific and Technological Innovation Cooperation (2021YFE0116700), the Shanghai Natural Science Foundation (20ZR1464400) and the Shanghai Sailing Program (22YF1455300).

References

1. O. A. Hurricane, P. K. Patel, R. Betti, D. H. Froula, S. P. Regan, S. A. Slutz, M. R. Gomez, and M. A. Sweeney, Rev. Mod. Phys. **95**, 025005 (2023).
2. R. S. Craxton, K. S. Anderson, T. R. Boehly, V. N. Goncharov, D. R. Harding, J. P. Knauer, R. L. McCrory, P. W. McKenty, D. D. Meyerhofer, J. F. Myatt, A. J. Schmitt, J. D. Sethian, R. W. Short, S. Skupsky, W. Theobald, W. L. Kruer, K. Tanaka, R. Betti, T. J. B. Collins, J. A. Delettrez, S. X. Hu, J. A. Marozas, A. V. Maximov, D. T. Michel, P. B. Radha, S. P. Regan, T. C. Sangster, W. Seka, A. A. Solodov, J. M. Soures, C. Stoeckl, and J. D. Zuegel, Phys. Plasmas **22**, 110501 (2015).
3. H. Abu-Shawareb, R. Acree, P. Adams, *et al.*, Phys. Rev. Lett. **132**, 065102 (2024).
4. R. Betti and O. A. Hurricane, Nat. Phys. **12**, 435 (2016).
5. W. L. Kruer, *The Physics of Laser Plasma Interactions* (Addison-Wesley Publishing, 1988).
6. R. E. Kidder, Nucl. Fusion **21**, 145 (1981).
7. D. Juraszek, in *Advanced Diagnostics for Magnetic and Inertial Fusion*, P. E. Stott, A. Wootton, G. Gorini, E. Sindoni, and D. Batani, eds. (Springer US, Boston, MA, 2002), pp. 11–18.
8. P. M. Celliers, G. W. Collins, L. B. Da Silva, D. M. Gold, and R. Cauble, Appl. Phys. Lett. **73**, 1320 (1998).
9. J. D. Kilkenny, W. W. Hsing, S. H. Batha, G. A. Rochau, T. C. Sangster, P. M. Bell, D. K. Bradley, H. Chen, J. A. Frenje, M. Gatu-Johnson, V. Y. Glebov, R. J. Leeper, A. J. Mackinnon, S. P. Regan, J. S. Ross, and J. l. Weaver, Rev. Sci. Instrum. **94**, 081101 (2023).
10. K. W. Hill, M. Bitter, P. C. Efthimion, R. Ellis, L. Gao, M. B. Schneider, H. Chen, S. Ayers, M. A. Barrios, P. Beiersdorfer, P. M. Bell, R. Bettencourt, D. K. Bradley, D. Casey, M. J. Edwards, B. A. Hammel, M. C. Hermann, W. W. Hsing, O. S. Jones, R. L. Kauffman, O. L. Landen, D. A. Liedahl, T. Ma, A. G. MacPhee, J. D. Moody, R. C. Nora, P. Patel, H. A. Scott, V. A. Smalyuk, B. K. Spears, D. B. THorn, J. D. Kilkenny, S. P. Regan, D. Nelson, R. Jungquist, I. Shoup, M. Y. Maron, and M. S. del Rio, in *26th IAEA Fusion Energy Conference* (2016), paper LLNL-PROC-704902.
11. P. M. Celliers and M. Millot, Rev. Sci. Instrum. **94**, 011101 (2023).
12. R. M. Malone, B. C. Frogget, M. I. Kaufman, T. W. Tunnell, R. L. Guyton, I. P. Reinbachs, P. W. Watts, J. R. Celeste, P. M. Celliers, T. L. Lee, B. J. MacGowan, E. W. Ng, R. B. Robinson, and L. G. Seppala, in *International Optical Design*, Technical Digest (CD) (Optica Publishing Group, 2006), paper ThA5.

13. A. M. Manuel, M. Millot, L. G. Seppala, G. Frieders, Z. Zeid, K. Christensen, and P. M. Celliers, Proc. SPIE **9591**, 959104 (2015).
14. Y. Yang, Y. Li, Z. Guan, C. Yang, S. Zhang, F. Wang, and T. Li, Opt. Commun. **456**, 124554 (2020).
15. P. M. Celliers, D. J. Erskine, C. M. Sorce, D. G. Braun, O. L. Landen, and G. W. Collins, Rev. Sci. Instrum. **81**, 035101 (2010).
16. R. F. Smith, J. H. Eggert, R. Jeanloz, T. S. Duffy, D. G. Braun, J. R. Patterson, R. E. Rudd, J. Biener, A. E. Lazicki, A. V. Hamza, J. Wang, T. Braun, L. X. Benedict, P. M. Celliers, and G. W. Collins, Nature **511**, 330 (2014).
17. F. A. Maryum, H. Allen, R. F. Smith, A. Jay, S. L. Zachary, and W. S. David, Proc. SPIE **8850**, 88500N (2013).
18. R. Malone, J. Bower, G. Capelle, J. Celeste, P. Celliers, B. Frogget, R. Guyton, M. Kaufman, G. Lare, T. Lee, B. MacGowan, S. Montelongo, E. Ng, Thomas, Jr., T. Tunnell, and P. Watts, Proc. SPIE **5523**, 148 (2004).
19. B. Kozioziemski, B. Bachmann, A. Do, and R. Tommasini, Rev. Sci. Instrum. **94**, 041102 (2023).
20. L. A. Pickworth, B. A. Hammel, V. A. Smalyuk, H. F. Robey, R. Tommasini, L. R. Benedetti, L. Berzak Hopkins, D. K. Bradley, M. Dayton, S. Felker, J. E. Field, S. W. Haan, B. Haid, R. Hatarik, E. Hartouni, D. Holunga, M. Hoppe, Jr., N. Izumi, S. Johnson, S. Khan, T. Kohut, B. Lahmann, O. L. Landen, S. LePape, A. G. MacPhee, E. Marley, N. B. Meezan, J. Milovich, S. R. Nagel, A. Nikroo, A. E. Pak, R. Petrasso, B. A. Remington, N. G. Rice, H. A. Scott, P. T. Springer, M. Stadermann, C. Walters, K. Widmann, and W. W. Hsing, Phys. Plasmas **25**, 082705 (2018).
21. A. B. Zylstra, D. T. Casey, A. Kritcher, L. Pickworth, B. Bachmann, K. Baker, J. Biener, T. Braun, D. Clark, V. Geppert-Kleinrath, M. Hohenberger, C. Kong, S. Le Pape, A. Nikroo, N. Rice, M. Rubery, M. Stadermann, D. Strozzi, C. Thomas, P. Volegov, C. Weber, C. Wild, C. Wilde, D. A. Callahan, and O. A. Hurricane, Phys. Plasmas **27**, 092709 (2020).
22. X. Liang, X. Xie, J. Kang, Q. Yang, H. Wei, M. Sun, and J. Zhu, High Power Laser Sci. Eng. **6**, e58 (2018).
23. J. Zhu, X. Xie, M. Sun, J. Kang, Q. Yang, A. Guo, H. Zhu, P. Zhu, Q. Gao, X. Liang, Z. Cui, S. Yang, C. Zhang, and Z. Lin, High Power Laser Sci. Eng. **6**, e29 (2018).
24. M. Sun, X. Xie, J. Zhu, X. Zhang, Y. Zhang, P. Zhu, A. Guo, J. Kang, H. Zhu, Q. Yang, and X. Liang, Appl. Opt. **60**, 2056 (2021).
25. P. Tzeferacos, M. Fatenejad, N. Flocke, C. Graziani, G. Gregori, D. Q. Lamb, D. Lee, J. Meinecke, A. Scopatz, and K. Weide, High Energy Density Phys. **17**, 24 (2015).
26. B. Fryxell, K. Olson, P. Ricker, F. X. Timmes, M. Zingale, D. Q. Lamb, P. MacNeice, R. Rosner, J. W. Truran, and H. Tufo, Astrophys. J. Suppl. Ser. **131**, 273 (2000).